

Title: Berry curvature memory via electrically driven stacking transitions

Jun Xiao^{1,2,8}, Ying Wang^{3,8}, Hua Wang⁴, C. D. Pemmaraju², Siqu Wang³, Philipp Muscher¹,
Edbert J. Sie^{2,5}, Clara M. Nyby⁶, Thomas P. Devereaux^{2,5}, Xiaofeng Qian⁴, Xiang Zhang^{3*} &
Aaron M. Lindenberg^{1,2,7*}

Affiliations:

¹ Department of Materials Science and Engineering, Stanford University, Stanford, CA 94305, USA.

² SIMES, SLAC National Accelerator Laboratory, Menlo Park, CA 94025, USA.

³ NSF Nanoscale Science and Engineering Center (NSEC), University of California at Berkeley, Berkeley, CA 94720, USA.

⁴ Department of Materials Science and Engineering, Texas A&M University, College Station, TX 77843, USA.

⁵ Geballe Laboratory for Advanced Materials, Stanford University, Stanford, CA 94305, USA.

⁶ Department of Chemistry, Stanford University, Stanford, CA, USA.

⁷ PULSE Institute, SLAC National Accelerator Laboratory, Menlo Park, CA, 94025, USA.

⁸ These authors contributed equally: Jun Xiao, Ying Wang

*Correspondence to: aaronl@stanford.edu; xiang@berkeley.edu

Abstract: In two-dimensional layered quantum materials, the interlayer stacking order determines both crystalline symmetry and quantum electronic properties such as Berry curvature, topology and electron correlation¹⁻⁴. Electrical stimuli can strongly influence¹⁻⁴ quasi-particle interactions and the free energy landscape^{5,6}, thus making it possible to access hidden stacking orders with novel quantum properties and enabling dynamic engineering of these attributes. Here we demonstrate electrically driven stacking transitions and a new type of nonvolatile memory based on Berry

curvature in few-layer WTe_2 . The interplay of out-of-plane electric fields and electrostatic doping controls in-plane interlayer sliding and creates multiple polar and centrosymmetric stacking orders. In-situ nonlinear Hall transport reveals such stacking rearrangements result in a layer-parity-selective Berry curvature memory in momentum space, where the sign reversal of the Berry curvature only occurs in odd layer crystals. Our findings open an avenue towards exploring coupling between topology, electron correlations, and ferroelectricity in hidden stacking orders and demonstrate a new low energy cost, electrically-controlled topological memory in the atomically thin limit.

Main

Berry curvature is a fundamental concept in condensed matter physics quantifying the topological local entanglement between conduction and valence bands in crystalline solids without time-reversal or space-inversion symmetry^{7,8}. This nonzero geometrical property of the band structure determines the anomalous motion of coherent electron wave packets and is a prerequisite for global topological invariants in quantum materials. Recently, the study of Berry curvature in layered van der Waals materials has attracted great attention, leading to many intriguing discoveries such as non-trivial topology in Weyl semimetals⁹, valleytronics in bulk 3R MoS_2 and topological transport in bilayer graphene domain walls^{3,10}. These findings indicate the fundamental role of layer stacking order, the relative crystallographic arrangement of atomic layers, in determining crystal symmetry and its enforced topological electronic properties. Recent findings on electron correlation and superconductivity in twisted bilayer graphene^{1,11}, further motivate the control of phase competition to access hidden stacking orders for novel physics and applications. Here we discover multiple stacking order transitions driven by electrical fields and doping in few layer WTe_2 . The transitions

among these phases through interlayer sliding enable synchronized annihilation and switching of the ferroelectric polarization and the Berry curvature. We further observe layer-parity-selective memory behavior of Berry curvature in momentum space, where the sign reversal of Berry curvature only occurs in odd layer crystals.

T_d phase WTe_2 is a layered material that crystallizes in a distorted hexagonal net with an orthorhombic unit cell (Fig. 1a). Prior theoretical studies have indicated that the WTe_2 can deviate from this equilibrium polar crystal structure to form different hidden stacking orders with distinct symmetries^{12,13}, including a non-polar monoclinic $1T'$ structure, and a polar orthorhombic T_d phase with upward spontaneous polarization (T_d, \uparrow) or downward spontaneous polarization (T_d, \downarrow). These three phases have same single-layer atomic configurations but distinct relative interlayer sliding along the b crystalline axis (Fig. 1a). The energy barrier for different stackings can be as small as few meV/unit cell¹⁴, about one to two orders of magnitude smaller than that for conventional bond rearrangement in phase-change materials^{15,16}. Therefore, electrical perturbation of ground state ordering is nontrivial and may drive proximal interlayer arrangements with unexplored physics and quantum properties. Further, as a type-II topological Weyl semimetal, T_d WTe_2 exhibits chiral Berry curvature monopoles^{9,17}. The arrangement of these positive and negative Berry curvature hotspots in momentum space leads to a nontrivial Berry curvature dipole (Fig. 1a), defined as $D_{ij} = -\int_k \Omega_j \partial_i f_0$ (Ω_j is the Berry curvature along the j direction and f_0 is the equilibrium electron distribution)¹⁸. Even down to the ultrathin limit, it maintains large Berry curvature and the associated dipole near the Fermi level^{19,20}. Therefore, WTe_2 is an ideal platform to demonstrate dynamic stacking transitions by electrical stimulus and its deterministic influence on Berry curvature and its dipole.

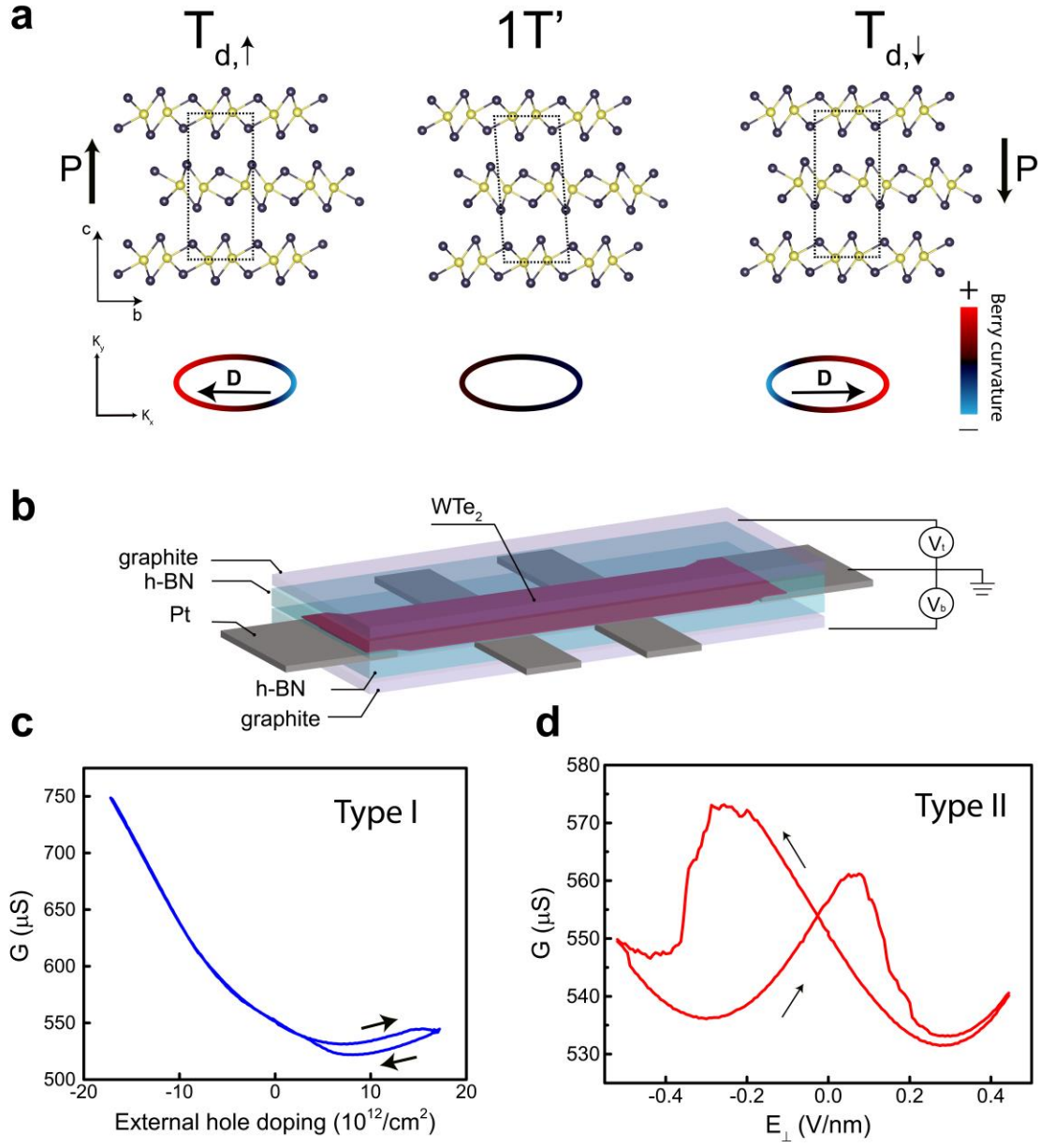


Figure 1 | Signatures of two different electrically-driven phase transitions in WTe_2 . **a**, Side view (b - c plane) of unit cell showing possible stacking orders in WTe_2 (monoclinic $1T'$, polar orthorhombic $T_{d,\uparrow}$ or $T_{d,\downarrow}$) and schematics of their Berry curvature distributions in momentum space. The yellow spheres refer to W atoms while the black spheres represent Te atoms. **b**, Schematic of dual-gate h-BN capped WTe_2 device. **c**, Electrical conductance G with rectangular-shape hysteresis (labeled as Type I) induced by external

doping at 80 K. Pure doping was applied following $V_t/d_t = V_b/d_b$ under a scan sequence indicated by black arrows. **d**, Electrical conductance G with butterfly-shape switching (labeled as Type II) driven by electric field at 80 K. Pure E field was applied following $-V_t/d_t = V_b/d_b$ under a scan sequence indicated by black arrows. Positive E_{\perp} is defined along $+c$ axis. Based on the distinct hysteresis observations in (c) and (d), two different phase transitions can be induced by different gating configurations.

To realize the electrical manipulation, we fabricated dual-gate devices based on few-layer WTe_2 encapsulated by two boron nitride (h-BN) flakes with thicknesses of d_t and d_b (Fig. 1b). The applied electric field passing upwards is $E_{\perp} = (-V_t/d_t + V_b/d_b)/2$, while the external hole doping is $n_h = -\epsilon_{\text{hBN}}\epsilon_0 (V_t/d_t + V_b/d_b)/e$. Two types of phase transitions can be induced by different gating configurations: under pure doping condition ($V_t/d_t = V_b/d_b$) in a five-layer sample, electrical conductance G shows a rectangular-shape hysteresis (labeled as Type I), appearing on the hole doping regime (Fig. 1c). In contrast, when only E_{\perp} is swept ($-V_t/d_t = V_b/d_b$), the electrical conductance shows a butterfly-shape response (labeled as Type II) and a bistability near zero bias (Fig. 1d).

To experimentally reveal the origin of the above two distinct phase transitions, we use *in-situ* gate-dependent second harmonic generation (SHG) and Raman spectroscopy. SHG is a sensitive probe to lattice asymmetry and space group in layered materials^{15,21}. A pristine T_d five-layer WTe_2 exhibits both strong SHG and the expected polarization pattern for Pm space group (Supplementary Fig. 1). We measure the SHG variation correlated with Type I electrical conductance under pure external doping sweeping (Fig. 2a). Accompanying an abrupt electrical conductance change at hole doping $\sim 1.5 \times 10^{13}/\text{cm}^2$, the SHG intensity shows a sharp decrease by a factor of five leaving a residue comparable to the background SHG from h-BN and graphite

(Supplementary Fig. 1c). This indicates the formation of a centrosymmetric phase prohibiting SHG, with measured threshold doping level consistent with prior theoretical predictions for a transition into 1T' stacking¹². The metastable nature of this induced phase results in a constant low SHG intensity during the retraction of carrier doping. At a lower hole doping level of $0.4 \times 10^{13}/\text{cm}^2$, we observe a rapid increase back to the initial intensity level of the T_d phase. We also find that a single gate bias providing electrostatic doping and additional electric field can trigger Type I hysteresis in both electrical conductance and SHG with lower hole doping requirement (Supplementary Fig. 2). We further observe the SHG modulation depth during the transition has strong layer dependence (Fig. 2b). With similar initial SHG intensity in T_d phase, the SHG drop is much more significant in trilayer and five-layer samples compared with that in four-layer samples. Such layer dependence is in line with the layer dependent crystalline symmetry of 1T' stacking²², i.e. the space group of even-layer 1T' WTe₂ is P_m without inversion symmetry leading to nontrivial SHG intensity and hence small SHG modulation. On the other hand, odd-layer 1T' WTe₂ belongs to the $P2_1/m$ space group with inversion symmetry resulting in the large SHG intensity change.

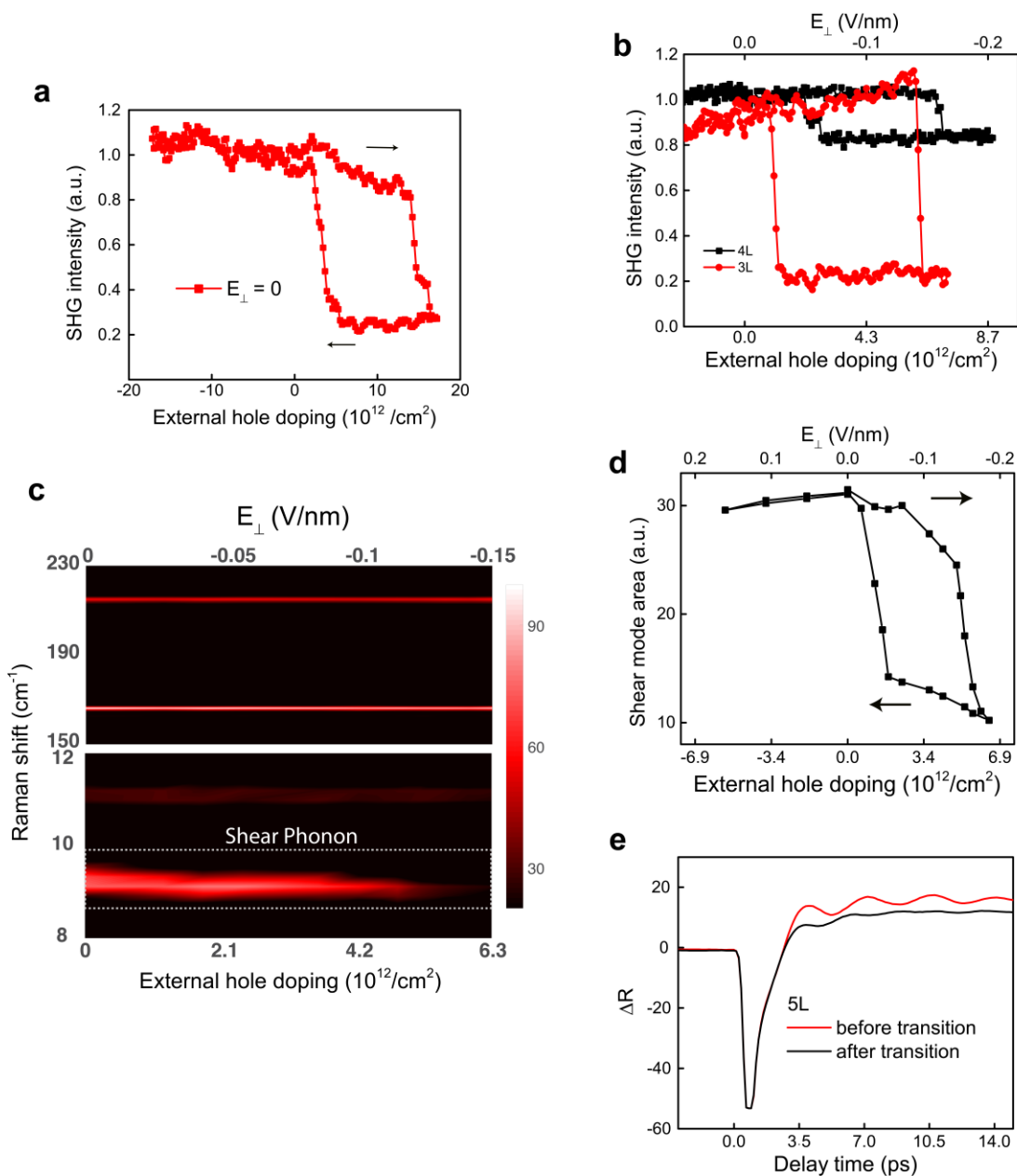


Figure 2 | Observation of interlayer sliding transition between T_d and $1T'$ stacking orders as the origin for Type I hysteresis. **a, A rectangular-shape SHG hysteresis with deep SHG modulation depth under pure doping sweep is observed (black arrows indicate the sweeping direction), correlated with Type I conductance hysteresis in fig 1c. The hole doping side is more favorable to drive the transition. **b**, Layer dependent modulation depth in rectangular-shape SHG hysteresis. The SHG drop is much larger in odd-**

layer compared with that in even-layer crystals. Such SHG contrast of the electrically induced state is in line with the layer dependent inversion symmetry preservation and breaking for few-layer 1T' stacking. **c**, Raman spectra evolution of intralayer and interlayer vibrations during Type I phase transition in five-layer WTe₂. Intralayer vibrations (165 and 215 cm⁻¹) display negligible modulation in intensity and frequency. In contrast, significant intensity reduction of the *b* axis interlayer shear mode (9 cm⁻¹) was observed, consistent with the formation of centrosymmetric 1T' stacking in this five-layer sample. **d**, Integrated area of such interlayer shear mode shows hysteresis response corresponding to the Type I transition. **e**, Coherent shear phonon dynamics in a five-layer device showing disappearance of coherent shear phonon vibrations after the transition. Together this shows that the origin of Type I phase change is a stacking transition between T_d and 1T' through interlayer sliding along the crystalline *b* axis, excluding any intralayer bond distortion or bond breaking.

Besides the observed symmetry transformation, we confirm such phase change is a stacking-order transition from T_d to 1T' through interlayer sliding as opposed to an intralayer bond distortion or bond breaking by *in-situ* gate-dependent Raman spectroscopy and coherent phonon dynamics. The inversion symmetry breaking in T_d phase allows a Raman-active interlayer shear mode corresponding to interlayer vibrations along the crystalline *b* axis (~9 cm⁻¹ at 80 K). The peak around 11 cm⁻¹ is attributed to a breathing mode while the other higher frequency peaks originate from intralayer vibrations within each atomic layer (Fig. 2c and Supplementary Fig. 3)²³. Unlike the even-parity breathing mode, the odd-parity shear mode is expected to vanish in a centrosymmetric state like 1T' stacking²⁴. Indeed, we observe a substantial intensity reduction of the interlayer shear mode in a five-layer sample during the Type I transition (Fig. 2c). Meanwhile, a negligible modulation in other high frequency intralayer vibration modes is observed. The gate dependent intensity of the shear mode further shows rectangular-shape hysteresis response

corresponding to the Type I structural phase transition (Fig. 2d). In complementary coherent phonon dynamics measurements (Fig. 2e), we again observe the disappearance of the shear mode in the time domain after formation of the centrosymmetric phase in a five-layer device. The recovery of inversion symmetry is expected for the well-known 1T' monoclinic stacking as well as a subtle variation recently proposed under nonequilibrium optical pumping²⁵. Taken together, the above evidence indicates the Type I phase change origin is a stacking transition between T_d and 1T' through interlayer sliding along the crystalline *b* axis, without any intralayer bond distortion or bond breaking.

Next we uncover the origin of Type II phase transition driven by pure electric field. The corresponding SHG measurement shows butterfly-shape intensity hysteresis in both a four-layer and a five-layer samples (Fig. 3a). This observation reflects the switching between ferroelectric polarizations, similar to that reported in prototypical ferroelectric oxides²⁶. However, the intensity minima at the turning points in four-layer and five-layer crystals show significant difference in magnitude, similar to the layer dependent SHG contrast in 1T' stacking. This shows that stacking structure changes take place in this ferroelectric switching process, which may involve 1T' stacking as the intermediate transition state *via* interlayer sliding. To identify the stacking order nature of fully poled upward and downward polarization phases in the Type II transition, we studied their characteristic lattice excitations. The two phases show the similar Raman frequency and amplitude of shear mode as well as high frequency vibrations belonging to polar T_d crystal geometry (Fig. 3b). In addition, the corresponding SHG polarization patterns are almost identical in terms of both pattern types and lobe orientations (Fig. 3c). These findings reveal that the Type II phase transition is a ferroelectric stacking switching between T_{d, ↑} and T_{d, ↓} orders, which also

explains the unknown microscopic origin for similar conductance phenomena reported in a recent study²⁷. The larger sliding displacement to switch these T_d phases thus leads to the observed larger electric field requirement (~ 0.4 V/nm) for fully poling, which is about 1.5-2.0 times higher than that applied in the formation of the intermediate stacking.

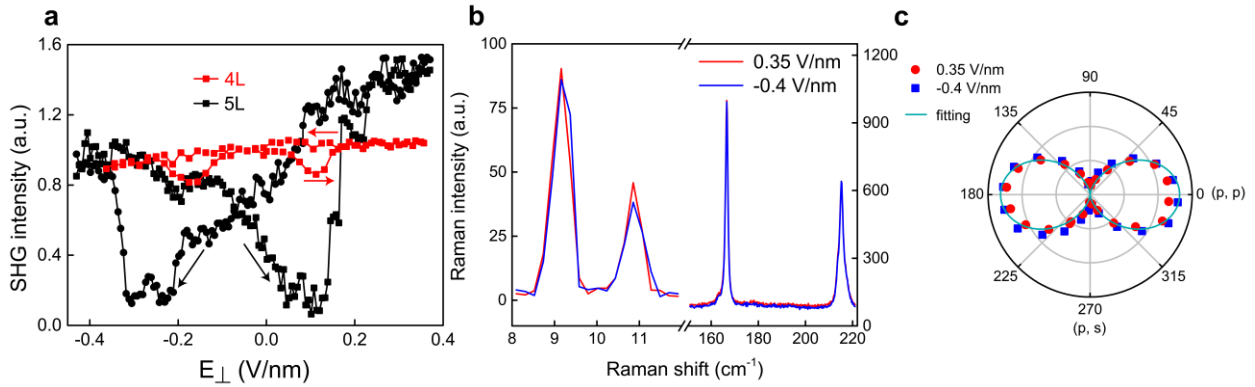


Figure 3 | Transition between $T_{a,\uparrow}$ and $T_{a,\downarrow}$ stacking orders with preservation of crystal orientation in

Type II hysteresis. a, *in-situ* SHG intensity evolution in Type II phase transition, driven by a pure E field sweep on a four-layer and a five-layer T_d -WTe₂ devices (indicated by the black arrows). Both show butterfly-shape SHG intensity hysteresis responses as a signature of ferroelectric switching between upward and downward polarization phases. The intensity minima at turning points in four-layer and five-layer crystals show significant difference in magnitude, consistent with the layer dependent SHG contrast in 1T' stacking. This suggests changes in stacking structures take place during the Type II phase transition, which may involve 1T' stacking as the intermediate state. **b**, Raman spectra of both interlayer and intralayer vibrations of fully poled upward and downward polarization phases in the 5L sample, showing nearly identical characteristic phonons of polar T_d crystals. **c**, SHG intensity of fully poled upward and downward polarization phases as a function of analyzer polarization angle, with fixed incident polarization along p direction (or b axis). Both the polarization patterns and lobe orientations of these two phases are almost the same and can be well fitted based on the second order susceptibility matrix of Pm space group

(Supplementary Information Section I). These observations reveal the transition between $T_{d, \uparrow}$ and $T_{d, \downarrow}$ stacking orders is the origin of Type II phase transition, through which the crystal orientations are preserved.

In the following, we now show how such electrically driven stacking transitions enable layer-parity selective memory behavior of Berry curvature and Berry curvature dipole (BCD) by nonlinear Hall effect (NHE). Since the nonlinear Hall signal is proportional to the Berry curvature dipole strength¹⁸, NHE has recently been identified as a hallmark to probe Berry curvature and its distribution in momentum space in time-reversal-invariant materials¹⁹. To capture the maximum nonlinear Hall response from the intrinsic Berry curvature dipole²⁰, the geometry of metal contacts is designed to allow current flow along the a axis and generate nonlinear Hall voltage along the b axis (Fig. 4a and Supplementary Fig. 4). Figure 4b shows the expected quadratic power relationship between applied AC current along a axis ($I_{//,\omega}$) and its 2nd harmonic transverse voltage along b axis ($V_{\perp,2\omega}$). The second-harmonic transverse response $V_{\perp,2\omega}$ is on the order of 0.1% of $V_{//,\omega}$. The associated Berry curvature dipole along a axis, $D_{ac} = -\int_k \Omega_c \partial_a f_0$, is proportional to $V_{\perp,2\omega} / (V_{//,\omega})^2$ and estimated to be on the order of $\sim 1 \text{ \AA}$ (Supplementary Information Section VII), which is consistent with prior reports²⁰. Between the $T_{d, \uparrow}$ and $T_{d, \downarrow}$ transitions, the conductance G and NHE signal $V_{\perp,2\omega} / (V_{//,\omega})^2$ in both trilayer and four-layer WTe₂ shows a clear hysteresis (Fig. 4c and d). Intriguingly, there is a sign switching of the NHE signal in the trilayer (Fig. 4c), indicating the proportional in-plane Berry curvature dipole also reverses its direction and possesses binary memory switching property. In contrast, the sign of NHE hysteresis signal is invariant in the four-layer WTe₂ (Fig. 4d). This layer parity dependence of sign switching is further evidenced by first-principles calculations of Berry curvature for trilayer and four-layer WTe₂ (Fig. 4f, g and Supplementary Fig. 5).

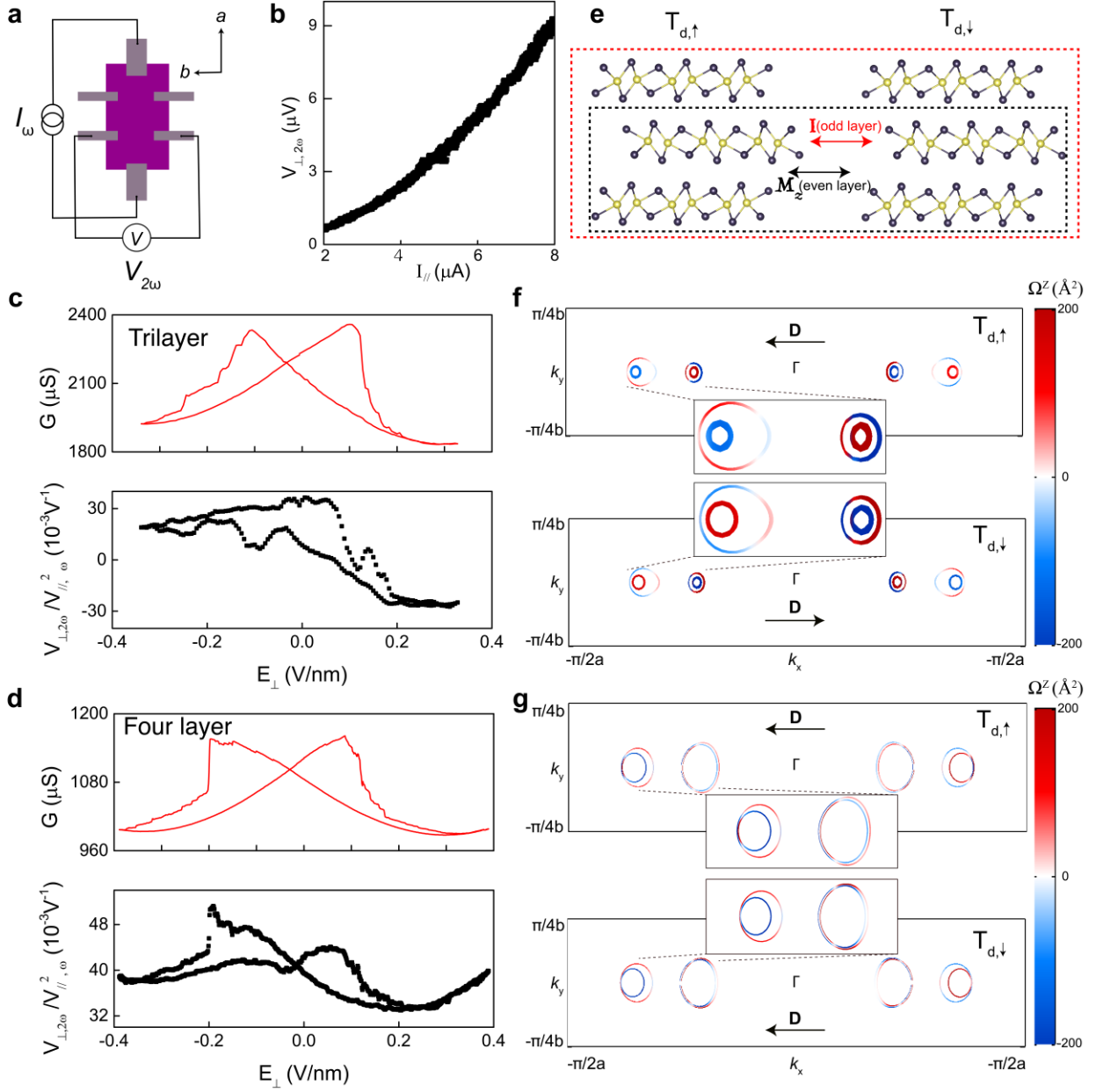


Fig. 4| Layer-parity selective memory behavior of Berry curvature during transitions between $T_{d,\uparrow}$ and $T_{d,\downarrow}$ stacking orders. **a**, The nonlinear Hall effect (NHE) measurement schematics. An applied current flow along the a axis results in the generation of nonlinear Hall voltage along the b axis, proportional to the Berry curvature dipole strength at the Fermi level. **b**, Quadratic amplitude of nonlinear transverse voltage at 2ω as a function of longitudinal current at ω . **c**, **d**, Electric field dependent longitudinal conductance (upper figure) and NHE (lower figure) in trilayer WTe_2 and four-layer WTe_2 respectively. Though similar butterfly-shape hysteresis in longitudinal conductance are observed, the sign of NHE was observed to be

reversed in the trilayer while maintaining unchanged in the four-layer crystal. Because NHE signal ($V_{\perp,2\omega} / (V_{\parallel,\omega})^2$) is proportional to Berry curvature dipole strength, it indicates the flipping of Berry curvature dipole only occurs in trilayer. **e**, Schematics of layer-parity selective symmetry operations effectively transforming $T_{d,\uparrow}$ to $T_{d,\downarrow}$. The interlayer sliding transition between these two ferroelectric stackings is equivalent to an inversion operation in odd layer while a mirror operation respect to the ab plane in even layer. **f, g**, Calculated Berry curvature Ω^z distribution in 2D Brillouin zone at the Fermi level for T_d (upper figure) and the corresponding flipped T_d phase (lower figure) in trilayer and four-layer WTe_2 . The symmetry operation analysis and first principle calculations confirm Berry curvature and its dipole sign reversal in trilayer while invariant in four-layer, leading to the observed layer-parity selective NHE memory behavior.

We discover this striking layer dependent reversal of Berry curvature dipole originating from the layer dependent symmetry operation during the transition from ferroelectric $T_{d,\uparrow}$ to $T_{d,\downarrow}$ states and the pseudovector character of the Berry curvature²⁸. Although $T_{d,\uparrow}$ and $T_{d,\downarrow}$ stackings are physically formed by different interlayer sliding, they are effectively related to each other via symmetry operations depending on layer number parity. In particular, the relation is an inversion operation for odd-layer WTe_2 , while a mirror operation with respect to the ab plane and a global half unit-cell translation along the a axis for even layers (Fig. 4e). As a consequence, the out-of-plane Berry curvature pseudovector in odd-layer inverts its direction while it maintains the same sign in even-layer for each transition between these two stacking orders. This directly leads to the layer parity selective reversal of Berry curvature dipole and NHE signal. Besides the substantial difference in initial and final ferroelectric stackings, the Berry curvatures were found to move in momentum space during such ferroelectric stacking transition (Supplementary Movie 1), and a hysteresis of NHE was also observed in type I phase transition showing vanishing NHE response at induced $1T'$ stacking in a trilayer sample (Supplementary Fig. 6). These findings clearly

demonstrate the nontrivial evolution of the position and strength of Berry curvature in momentum space through stacking order transitions, enabling dynamic control of Berry curvatures and a memory storage property of the Berry curvature dipole. This new type of memory is expected to be highly energy-efficient. To overcome the small stacking barrier (few meV/unit cell), only ~ 0.1 aJ/nm² energy is estimated to be consumed for each stacking transition as a single “writing” operation. On the other hand, although $T_{d, \uparrow}$ and $T_{d, \downarrow}$ semimetal show little electrical conductance difference, the opposite sign of their large Berry curvature dipole in odd-layer allows for substantial contrast in NHE reading, enabling a non-destructive and nonmagnetic reading mechanism.

Conclusions

In summary, we report the first observation of electrically driven stacking transitions in few-layer WTe₂ and associated Berry curvature memory determined by layer number parity. We reveal the important role of electric fields and doping to create and stabilize hidden stacking orderings, thus diversifying the class of quantum materials. Our work further defines a new type of nonvolatile memory based on a quantum geometric property with non-destructive electrical reading in the atomically thin limit. Its low energy barrier theoretically sets an ultralow energy cost (~ 0.1 aJ/nm²) for each “writing” operation between multiple states, a significant improvement over current DRAM or chalcogenide phase change memory and appealing for future neuromorphic computing paradigms^{29–31}. Finally, the ability to control Berry curvature and crystal symmetry via stacking transitions may enable the exploration of the uncharted interplay between these degree of freedoms and recently proposed higher order topology with helical hinge states in layered materials³².

Methods

Device fabrication

The dual-gated few layer WTe_2 devices were fabricated in the following sequence: First, graphite and h-BN crystals were mechanically exfoliated onto 280 nm SiO_2/Si substrates. Graphite flakes 2–5 nm thick were chosen for the top and bottom gates and 10 - 30-nm-thick h-BN flakes were chosen for the top and bottom dielectric. The top and bottom parts were prepared separately using a polymer-based dry transfer technique. For the bottom part, an h-BN flake was picked up on a polymer stamp and placed on the bottom graphite. After dissolving the polymer, fine Pt metal contacts (~ 5 nm) were patterned on the h-BN. The surface was further cleaned by a 400 °C annealing process in high vacuum. For the top part, the graphite was picked up first, then the top h-BN. Both stacks were then transferred to an oxygen- and water-free glovebox. WTe_2 crystals were exfoliated inside the glovebox and flakes with suitable thickness identified by optical contrast were picked up with the top part; the stack was then completed by transferring onto contacts/h-BN/graphite stack before taking out of the glovebox. Finally, after dissolving the polymer, another step of e-beam lithography and metallization was used to define electrical bonding pads (Cr/Au) connecting to the metal contacts and the top and bottom gates. The layer number of WTe_2 and thickness of BN were confirmed by Raman spectroscopy and AFM²³.

SHG, Raman spectroscopy and coherent phonon pump-probe dynamics

SHG spectroscopy: The excitation light centered at 810 nm was extracted from a mode-locked 80 MHz titanium-sapphire oscillator. The laser was focused with a 40X long working distance objective on the sample located in a continuous-flow liquid-nitrogen cryostat. The SHG signal was detected in a backscattering configuration and finally collected by a single-photon PMT counter

from Hamamatsu with suitable bandpass filters. In all gate dependent SHG measurements, the excitation light polarization is along b axis without analyzer. The excitation light incidence angle is at either 0 degree (normal incidence) or 30 degree (oblique incidence). In SHG polarization pattern measurements, s polarization is along the a axis while p polarization is along the b axis. All SHG measurements were conducted at 80 K unless explicitly noted.

Raman spectroscopy was performed using a commercial Raman system (Horiba Labram HR Evolution) using a helium-neon laser ($\lambda = 632.8$ nm) at normal incidence. The system is installed with a ULF module to allow detection of ultralow Raman scattering down to 7 cm^{-1} . The laser beam was focused with a spot size ~ 1.5 μm on the samples by a 40 X long working distance objective with a correction ring (N.A. = 0.6); The samples were located in a continuous-flow liquid-nitrogen cryostat which can be cooled down to 78 K in a vacuum of 10^{-5} mbar. A polarized Raman measurement was achieved by using a visible half-wave plate mounted on a motorized stage before the objective. The incident polarization of the linear polarized laser can be accurately controlled by rotating the half-wave plate. The Raman signal was collected in a reflection configuration without an extra polarizer and detected using a charge-coupled device. All Raman measurements were conducted at 80 K unless explicitly noted.

A non-degenerate pump-probe setup was used to study the coherent phonon dynamics in few-layer WTe_2 devices. The pump beam (~ 1300 nm) is from an optical parametric oscillator (OPO) pumped by a mode-locked titanium-sapphire oscillator while the probe beam (~ 810 nm) is from the same titanium-sapphire oscillator. The pump beam was modulated by a chopper at a frequency of 2 kHz and focused onto the sample to excite coherent phonons, while the reflectivity change of the probe

beam was measured by a silicon-based photodetector coupled to a SR830 lock-in amplifier. The excited coherent phonons can modulate the optical susceptibility at the phonon frequency, which result in corresponding reflectivity oscillations of the probe beam. We keep the pump fluence at about $300 \mu\text{J}/\text{cm}^2$, 10 times stronger than the probe pulses.

Gate dependent nonlinear Hall measurements

Electrical transport was measured in a continuous-flow liquid-nitrogen cryostat. The top and bottom gate voltages were applied through two Keithley 2450 sourcemeters. First- and second-harmonic signals were collected simultaneously by standard lock-in techniques by two SR830 lock-in amplifiers with excitation frequency at 50 Hz. The phase of the first-harmonic (second-harmonic) signal was approximately 0° ($\pm 90^\circ$), consistent with the expected values for first- and second-order responses. All electrical measurements were conducted at 80 K unless explicitly noted.

First-principles electronic structure calculations

First-principles density functional theory was applied for structural relaxation and electric polarization calculation using Vienna Ab initio Simulation Package (VASP) with the Perdew-Burke-Ernzerhof exchange-correlation functional^{33,34}, a plane-wave basis with cutoff of 300 eV, a $6 \times 12 \times 1$ Monkhorst-Pack k-point sampling, and optB88-vdW functional for interlayer van der Waals interactions³⁵. Furthermore, to compute Berry curvature, we developed first-principles tight-binding Hamiltonian in the quasiatomic Wannier function basis set based on the maximal similarity measure^{36,37}. Here we include spin-orbit coupling and adopt HSE06 hybrid exchange-correlation energy functional with the range-separation parameter $\lambda = 0.2$ ³⁸. Using the above

approach, we then developed effective tight-binding Hamiltonian for trilayer and four-layer WTe₂ with total 168 and 224 quasiautomatic Wannier functions, respectively. Berry curvature was subsequently calculated with a dense k-point sampling of 300×300×1.

References:

1. Cao, Y. *et al.* Correlated insulator behaviour at half-filling in magic-angle graphene superlattices. *Nature* **556**, 80–84 (2018).
2. Soluyanov, A. A. *et al.* Type-II Weyl semimetals. *Nature* **527**, 495–498 (2015).
3. Ju, L. *et al.* Topological valley transport at bilayer graphene domain walls. *Nature* **520**, 650–655 (2015).
4. Chen, G. *et al.* Evidence of a gate-tunable Mott insulator in a trilayer graphene moiré superlattice. *Nat. Phys.* **15**, 237–241 (2019).
5. Wang, J., Lian, B. & Zhang, S.-C. Electrically Tunable Magnetism in Magnetic Topological Insulators. *Phys. Rev. Lett.* **115**, 036805 (2015).
6. Li, Y., Duerloo, K.-A. N., Wauson, K. & Reed, E. J. Structural semiconductor-to-semimetal phase transition in two-dimensional materials induced by electrostatic gating. *Nat. Commun.* **7**, 10671 (2016).
7. Haldane, F. D. M. Nobel Lecture: Topological quantum matter. *Rev. Mod. Phys.* **89**, 040502 (2017).
8. Yan, B. & Felser, C. Topological Materials: Weyl Semimetals. *Annu. Rev. Condens. Matter Phys.* **8**, 337–354 (2017).
9. Armitage, N. P., Mele, E. J. & Vishwanath, A. Weyl and Dirac semimetals in three-dimensional solids. *Rev. Mod. Phys.* **90**, 015001 (2018).
10. Suzuki, R. *et al.* Valley-dependent spin polarization in bulk MoS₂ with broken inversion symmetry. *Nat. Nanotechnol.* **9**, 611–617 (2014).

11. Cao, Y. *et al.* Unconventional superconductivity in magic-angle graphene superlattices. *Nature* **556**, 43–50 (2018).
12. Kim, H.-J., Kang, S.-H., Hamada, I. & Son, Y.-W. Origins of the structural phase transitions in MoTe_2 and WTe_2 . *Phys. Rev. B* **95**, 180101 (2017).
13. Yang, Q., Wu, M. & Li, J. Origin of Two-Dimensional Vertical Ferroelectricity in WTe_2 Bilayer and Multilayer. *J. Phys. Chem. Lett.* **9**, 7160–7164 (2018).
14. Lu, P. *et al.* Origin of superconductivity in the Weyl semimetal WTe_2 under pressure. *Phys. Rev. B* **94**, 224512 (2016).
15. Xiao, J. *et al.* Intrinsic Two-Dimensional Ferroelectricity with Dipole Locking. *Phys. Rev. Lett.* **120**, 227601 (2018).
16. Zhang, W., Mazzarello, R., Wuttig, M. & Ma, E. Designing crystallization in phase-change materials for universal memory and neuro-inspired computing. *Nat. Rev. Mater.* **4**, 150–168 (2019).
17. Soluyanov, A. A. *et al.* Type-II Weyl semimetals. *Nature* **527**, 495 (2015).
18. Sodemann, I. & Fu, L. Quantum Nonlinear Hall Effect Induced by Berry Curvature Dipole in Time-Reversal Invariant Materials. *Phys. Rev. Lett.* **115**, 216806 (2015).
19. Ma, Q. *et al.* Observation of the nonlinear Hall effect under time-reversal-symmetric conditions. *Nature* **565**, 337–342 (2019).
20. Kang, K., Li, T., Sohn, E., Shan, J. & Mak, K. F. Nonlinear anomalous Hall effect in few-layer WTe_2 . *Nat. Mater.* **18**, 324–328 (2019).
21. Wang, Y., Xiao, J., Yang, S., Wang, Y. & Zhang, X. Second harmonic generation spectroscopy on two-dimensional materials [Invited]. *Opt. Mater. Express* **9**, 1136 (2019).
22. Beams, R. *et al.* Characterization of Few-Layer 1T' MoTe_2 by Polarization-Resolved Second Harmonic Generation and Raman Scattering. *ACS Nano* **10**, 9626–9636 (2016).
23. Kim, M. *et al.* Determination of the thickness and orientation of few-layer tungsten ditelluride using

- polarized Raman spectroscopy. *2D Mater.* **3**, 034004 (2016).
24. Chen, S.-Y., Goldstein, T., Venkataraman, D., Ramasubramaniam, A. & Yan, J. Activation of New Raman Modes by Inversion Symmetry Breaking in Type II Weyl Semimetal Candidate T' -MoTe₂. *Nano Lett.* **16**, 5852–5860 (2016).
 25. Sie, E. J. *et al.* An ultrafast symmetry switch in a Weyl semimetal. *Nature* **565**, 61–66 (2019).
 26. Varga, T. *et al.* Coexistence of Weak Ferromagnetism and Ferroelectricity in the High Pressure LiNbO_3 - Type Phase of FeTiO_3 . *Phys. Rev. Lett.* **103**, 047601 (2009).
 27. Fei, Z. *et al.* Ferroelectric switching of a two-dimensional metal. *Nature* **560**, 336–339 (2018).
 28. Wang, H. & Qian, X. Ferroelectric nonlinear anomalous Hall effect in few-layer WTe₂. *Arxiv: 1909.03610* (2019).
 29. Rehn, D. A., Li, Y., Pop, E. & Reed, E. J. Theoretical potential for low energy consumption phase change memory utilizing electrostatically-induced structural phase transitions in 2D materials. *npj Comput. Mater.* **4**, 2 (2018).
 30. Wong, H.-S. P. & Salahuddin, S. Memory leads the way to better computing. *Nat. Nanotechnol.* **10**, 191–194 (2015).
 31. Zidan, M. A., Strachan, J. P. & Lu, W. D. The future of electronics based on memristive systems. *Nat. Electron.* **1**, 22–29 (2018).
 32. Wang, Z., Wieder, B. J., Li, J., Yan, B. & Bernevig, B. A. Higher-Order Topology, Monopole Nodal Lines, and the Origin of Large Fermi Arcs in Transition Metal Dichalcogenides XTe_2 ($\text{X} = \text{Mo}, \text{W}$). *Phys. Rev. Lett.* **123**, 186401 (2019).
 33. Perdew, J. P., Burke, K. & Ernzerhof, M. Generalized Gradient Approximation Made Simple. *Phys. Rev. Lett.* **77**, 3865–3868 (1996).
 34. Kresse, G. & Furthmüller, J. Efficient iterative schemes for *ab initio* total-energy calculations using a plane-wave basis set. *Phys. Rev. B* **54**, 11169–11186 (1996).

35. Klimeš, J., Bowler, D. R. & Michaelides, A. Chemical accuracy for the van der Waals density functional. *J. Phys. Condens. Matter* **22**, 022201 (2010).
36. Qian, X. *et al.* Quasiatomic orbitals for *ab initio* tight-binding analysis. *Phys. Rev. B* **78**, 245112 (2008).
37. Marzari, N., Mostofi, A. A., Yates, J. R., Souza, I. & Vanderbilt, D. Maximally localized Wannier functions: Theory and applications. *Rev. Mod. Phys.* **84**, 1419–1475 (2012).
38. Krukau, A. V., Vydrov, O. A., Izmaylov, A. F. & Scuseria, G. E. Influence of the exchange screening parameter on the performance of screened hybrid functionals. *J. Chem. Phys.* **125**, 224106 (2006).

Acknowledgments:

This work is supported by the US Department of Energy (DOE), Office of Basic Energy Sciences, Division of Materials Sciences and Engineering, under contract number DE-AC02-76SF00515 (J.X., E.J.S., C.M.N., P.M., C.D.P., T.P.D., A.M.L.). E.J.S. acknowledges additional support from Stanford GLAM Postdoctoral Fellowship Program. C.M.N. acknowledges additional support from the National Science Foundation (NSF) through a Graduate Research Fellowship (DGE-114747). H.W. and X.Q. acknowledge the support by the National Science Foundation (NSF) under award number DMR-1753054. First-principles electronic structure and Berry curvature calculations by H.W. and X.Q. were conducted with the advanced computing resources provided by Texas A&M High Performance Research Computing.